

Influence of Active Nano Particle Size and Material Composition on Multiple Quantum Emitter Enhancements: Their Enhancement and Jamming Effects

Samel Arslanagić^{1, *} and Richard W. Ziolkowski²

(Invited Paper)

Abstract—In the 150 years that scientists and engineers have used Maxwell’s equations to describe electromagnetic phenomena, canonical scattering and radiating problems have played a very important role, providing explanations of and insights into their underlying physics. With the same intent, a variety of active coated nano-particles are examined here theoretically with regard to their ability to effectively enhance or jam the responses of quantum emitters, e.g., fluorescing molecules, and nano-antennas to an observer located in their far-field regions. The investigated spherical particles consist of a gain-impregnated silica nano-core covered with a nano-shell of a specific plasmonic material. Attention is devoted to the influence of the over-all size of these particles and their material composition on the obtained levels of active enhancement or jamming. Silver, gold and copper are employed as their nano-shells. The over-all diameters of the investigated coated nano-particles are taken to be 20 nm, 40 nm, and 60 nm, while maintaining the same ratio of the core radius and shell thickness. It is shown that the jamming levels, particularly when several emitters are present, are significantly larger for particles of larger sizes. These configurations are also shown to lead to the largest enhancement levels of the surrounding quantum emitters. Furthermore, for a fixed particle size and for a gain constant that produces the largest enhancement peak at optical wavelengths, it is demonstrated that these larger levels are most notable when the nano-shell is gold.

1. INTRODUCTION

Plasmonic materials, such as gold and silver, possess a negative real part of the permittivity at optical frequencies. They are useful, for instance, for the synthesis of optical metamaterials [1, 2] and optical antennas [3, 4] for local field enhancements. One of the major factors limiting the performance of plasmonic-based structures is, however, the large absorption loss associated with these metals at optical frequencies. There have been a variety of proposals for introducing gain into plasmonic-based structures to overcome these losses [4, Chap. 4, 5–14]. Thus, these passive and active nano-systems are distinguishable by the presence of gain materials. When used in combination with dielectric materials, passive and active plasmonic-based structures offer interesting enhanced, as well as reduced scattering effects even when their overall sizes are electrically small. These effects are particularly noticeable with the active-based designs.

When the nano-shell of a coated spherical nano-particle (CNP) is a plasmonic material, novel optical properties, such as resonant scattering or transparency, can occur [5, 15, 16]. These properties

Received 2 July 2014, Accepted 1 September 2014, Scheduled 6 September 2014

Invited paper for the Commemorative Collection on the 150-Year Anniversary of Maxwell’s Equations.

* Corresponding author: Samel Arslanagić (sar@elektro.dtu.dk).

¹ Department of Electrical Engineering, Technical University of Denmark, Ørsteds Plads, Bldg. 348, Kgs. Lyngby 2800, Denmark.

² Department of Electrical and Computer Engineering, University of Arizona, 1230 E. Speedway Blvd., Tucson 85721-0104, USA.

have been considered, for instance, for nano-sensors to achieve enhanced non-invasive measurements of the electromagnetic properties of fluorescing molecules [17, 18], optical invisibility [19, 20], solar energy harvesting absorbers [21], and nano-antennas [3, 4, 22]. Moreover, recent reviews [23, 24] clearly stress the importance of plasmonic-based nano-particles and their potential for a variety of biomedical applications. These include the sensing, characterization and imaging of tissues for early cancer detection and even efficient drug delivery. Plasmon-based nano-sensors have also been studied for a variety of other chemical and biological applications [25].

While many nano-particle configurations have been examined under plane wave excitations, the radiating properties of highly sub-wavelength, resonant, passive and active spherical CNPs have also been studied under electric Hertzian dipole (EHD) excitations [4, Chap. 4, 26–29]. In addition to significantly enhancing the total power radiated by a single EHD [4, Chap. 4, 27, 28], active CNP configurations have been found that significantly decrease it [4, Chap. 4, 29]. Both extremes can be exploited effectively for nano-sensor applications. Because the resonance frequencies of the CNPs can be tuned geometrically, CNPs can be designed to enhance particular molecular emission lines and to suppress others. Active CNP-based enhancement phenomena have been examined for a single EHD excitation [4, Chap. 4, 27] and with varying CNP sizes and constituent plasmonic materials [4, Chap. 4, 28]. The associated jamming phenomena were examined in different EHD environments (1, 2, or 4 EHDs), but for only one particular size of silver based CNPs (6 nm thick nano-shells) [4, Chap. 4, 29].

The present work extends these previous studies. It also further addresses the ability of a number of active CNPs, of different sizes and constituent plasmonic materials, to effectively enhance or jam the radiation from one or more quantum emitters, e.g., a set of fluorescing molecules. Moreover, it includes studies of the impact of the choice of plasmonic shell on these effects. The molecular emitters will be represented here by EHDs radiating at one of their resonance frequencies. This is a traditional treatment in semi-classical models [e.g., 30]. A short discussion will be included on the single and multiple EHD excitation cases to introduce the solution approach and to emphasize the associated basic physics. Attention is devoted to cases where one, two or four EHDs radiate simultaneously near to a properly designed active spherical CNP. In particular, the influence of the CNP size and material composition on the quantum emitter enhancement and jamming effects will be investigated. We assume that the EHDs emit coherently. Since all the emitters and the CNP are located within highly subwavelength distances of each other, this choice is reasonable. It also provides a maximum bound on the performance characteristics. It will be shown that the signals radiated by a single EHD or multiple EHDs can be significantly enhanced by the presence of an active CNP. Moreover, it will be demonstrated how the active CNP can also be used to suppress the total power radiated by these EHDs. Since the active CNP effectively blocks the power radiated by the EHDs from reaching the far field in those cases, we call this suppression process “jamming”. It will also be discussed how the power radiated in the multiple-EHD configurations is decreased even further than it is in the single EHD case. Furthermore, it will be shown that in all of the cases considered, more efficient enhancements and jamming require larger particle sizes and that the most profound enhancement and jamming results in the visible regime are associated with the gold-based CNP designs. The initial investigations of the far-field characteristics associated with the various excitations will use the magnitudes and directions of the power flow densities to shed more light on their particular behaviors.

This manuscript is organized as follows. In Section 2 the configuration of a CNP excited by one, two, or four EHDs is briefly described. Section 3 includes the necessary details of the analytical treatment. Section 4 is initiated by a brief account on the material and gain models used in the active CNP configuration. This discussion is then followed by a presentation of the highlighted numerical results. Finally, Section 5 summarizes and concludes the present work, and outlines ideas for its extensions. Throughout the manuscript, the time factor $\exp(j\omega t)$, with ω being the angular frequency, and t being the time, is assumed and suppressed.

2. CONFIGURATION AND THEORY

2.1. Configuration

The CNP of present interest is shown in Figure 1. It consists of a nano-core sphere (of radius r_1) coated concentrically with a nano-shell (of radius r_2), and located in free space. The nano-core and nano-shell

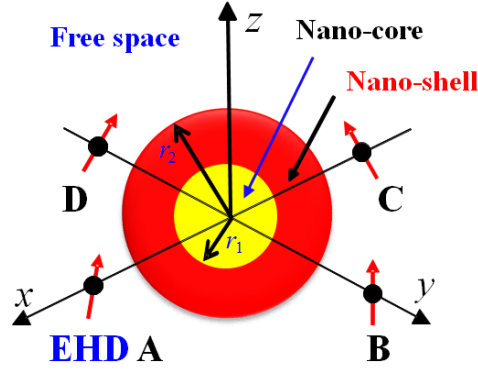


Figure 1. Multiple electric Hertzian dipoles (EHDs) illuminating a spherical CNP. The EHDs are represented by the black-colored circles; their orientations are represented by the red arrows. Three excitation cases are considered: Case 1 (EHD A), Case 2 (EHD A+C) and Case 3 (EHD A+B+C+D).

consist of simple materials with permittivities, permeabilities, and wave numbers, respectively, denoted by ε_1 , μ_1 , and k_1 , (for the nano-core) and ε_2 , μ_2 , and k_2 (for the nano-shell). The permittivity and permeability of the ambient free space are ε_0 and μ_0 . The free-space wave number and impedance are, respectively, $k_0 = \omega\sqrt{\varepsilon_0\mu_0}$ and $\eta_0 = \sqrt{\mu_0/\varepsilon_0}$. The CNP is excited by one or more EHDs, which constitute the standard dipole models of the quantum emitters. The EHDs are represented by the red arrows overlaid with the black circles and are labeled as A, B, C, and D in the figure. The EHDs can be arbitrarily oriented. The dipole (current) moment of the X th EHD, where $X = A, B, C$, and D , is given by $\vec{p}_X = \hat{p}_X p_X$, where the unit vector \hat{p}_X is its orientation and p_X [Am] is its complex amplitude. This work examines the same excitations of the CNP as those defined in [29]: Case 1, where only EHD A excites the CNP; Case 2, where EHDs A and C both excite the CNP; and Case 3, where all four EHDs excite the CNP simultaneously. A spherical coordinate system (r, θ, ϕ) and the associated rectangular coordinate system (x, y, z) are introduced so that their origins coincide with the center of the CNP. The coordinates of the X th EHD, $X = A, B, C$, and D , are denoted by $(r_{s,X}, \theta_{s,X}, \phi_{s,X})$. The EHDs are located symmetrically at positions in the xy -plane (i.e., for all X , $\theta_{s,X} = \pi/2$) outside of the CNP. In particular, EHDs A and C are on opposite sides of the CNP along the x -axis (i.e., $\phi_{s,A} = 0$, $\phi_{s,C} = \pi$), whereas EHDs B and D are on opposite sides along the y -axis (i.e., $\phi_{s,B} = \pi/2$, $\phi_{s,D} = 3\pi/2$). The radial distance of all of the EHDs from the CNP center is $r_{s,X} \equiv r_s = 40$ nm.

2.2. Theory

The analytical solution to the problem in Figure 1 was obtained in [26] for the single EHD case and summarized in [29] for the multiple EHD case. We state below the results of those solution procedures which are necessary for providing explanations to the main numerical results presented in a subsequent section.

The electric and magnetic fields due to any of the EHDs, EHD X ($X = A, B, C$ or D) are expanded in transverse magnetic (TM) and transverse electric (TE) spherical vector waves with known TM and TE expansion coefficients, denoted by $a_{X,nm}^{(c)}$ and $b_{X,nm}^{(c)}$, respectively. These fields constitute the known incident fields; the mathematical form of the electric field of the X th EHD is given by the following expression

$$\vec{E}_{\text{EHD},X} = \sum_{n=1}^{\infty} \sum_{m=-n}^n \frac{1}{j\omega\varepsilon_0\mu_0} a_{X,nm}^{(c)} \vec{N}_{nm}^{\text{TM},(c)} - \frac{1}{\varepsilon_0} b_{X,nm}^{(c)} \vec{M}_{nm}^{\text{TE},(c)}, \quad (1a)$$

where $\vec{N}_{nm}^{\text{TM},(c)}$ and $\vec{M}_{nm}^{\text{TE},(c)}$ are the familiar spherical vector wave functions (see e.g., Equations (2) and

(3) in [26]), and the known TM and TE expansion coefficients are given by the expressions

$$a_{X,nm}^{(c)} = -jk_0 \frac{p_X}{4\pi} \frac{1}{\mu_0} \frac{2n+1}{n(n+1)} \frac{(n-|m|)!}{(n+|m|)!} \{\hat{p}_X \cdot \vec{N}_{n,-m}^{(\text{TM}), (5-c)}(r_{s,X}, \theta_{s,X}, \phi_{s,X})\}, \quad (1b)$$

$$b_{X,nm}^{(c)} = \frac{k_0^3 p_X}{\omega} \frac{1}{4\pi} \frac{1}{\varepsilon_0^2} \frac{2n+1}{n(n+1)} \frac{(n-|m|)!}{(n+|m|)!} \{\hat{p}_X \cdot \vec{M}_{n,-m}^{(\text{TE}), (5-c)}(r_{s,X}, \theta_{s,X}, \phi_{s,X})\}. \quad (1c)$$

The index $c = 1$ applies to $r < r_s$ (where the radial behavior of the field is described by the spherical Bessel functions of order n , $j_n(\cdot)$, and their derivatives), while $c = 4$ applies to $r > r_s$ (where it is described by the spherical Hankel functions of the second kind and order n , $h_n^2(\cdot)$, and their derivatives). This choice of index c is made to coincide with the corresponding expansions of the unknown fields scattered from the CNP. The unknown scattered fields are also expanded in terms of the TM and TE spherical waves. These expansions differ, of course, in the radial behavior of the field. Inside the nano-core, the spherical Bessel functions ($c = 1$) of order n (and their derivatives) are used. Inside the nano-shell, the spherical Bessel ($c = 1$) and Neumann ($c = 2$) functions of order n , $y_n(\cdot)$, (and their derivatives) are used. Finally, outside of the CNP, the spherical Hankel ($c = 4$) functions of the second kind and order n (and their derivatives) are used[†]. The unknown coefficients in these expansions (denoted by $A_{i,nm}$ (for the TM coefficients) and $B_{i,nm}$ (for the TE coefficients), where $i = 1$ for the fields in the nano-core, $i = 2$ and 3 for the fields in the nano-shell, and $i = 4$ for the fields outside the CNP, follow by the application of the boundary conditions requiring the continuity of the tangential electric and magnetic field components at the two spherical interfaces of the CNP, i.e., at $r = r_1$ and $r = r_2$. Specifically, it can be shown that the expansion coefficients are determined from the following expression

$$\vec{D}_{nm} = \left(\vec{M}\right)^{-1} \vec{\Lambda}_{nm}, \quad (2)$$

where $\vec{D}_{nm} = [A_{1,nm}, \dots, A_{4,nm}, B_{1,nm}, \dots, B_{4,nm}]$ is the vector containing the unknown expansion coefficients and $\vec{\Lambda}_{nm} = [\Lambda_{\ell,nm}]$, $\ell = 1, \dots, 8$, is the excitation vector which depends on the source orientation and location. In the present work, all of the EHDs are outside the CNP; thus the incident fields that illuminate the CNP are those defined for $r < r_s$. Consequently, the excitation vector corresponds to the $c = 1$ case of the incident field. The corresponding elements of the excitation vector are summarized in Table 1 below.

Table 1. The elements, $\Lambda_{\ell,nm}$, $\ell = 1, \dots, 8$ of the excitation vector $\vec{\Lambda}_{nm}$ when the EHD is outside the CNP.

$\Lambda_{1,nm}$	$\Lambda_{2,nm}$	$\Lambda_{3,nm}$	$\Lambda_{4,nm}$	$\Lambda_{5,nm}$	$\Lambda_{6,nm}$	$\Lambda_{7,nm}$	$\Lambda_{8,nm}$
0	0	$a_{nm}^{(1)} j_n(k_0 r_2)$	$\frac{\varepsilon_2}{\varepsilon_0} a_{nm}^{(1)} d'_{r=r_2} \{r j_n(k_0 r)\}$	0	0	$b_{nm}^{(1)} j_n(k_0 r_2)$	$\frac{\mu_2}{\mu_0} b_{nm}^{(1)} d'_{r=r_2} \{r j_n(k_0 r)\}$

In Table 1, the coefficients take the form of

$$\begin{pmatrix} a_{nm}^{(1)} \\ b_{nm}^{(1)} \end{pmatrix} = \begin{pmatrix} a_{A,nm}^{(1)} \\ b_{A,nm}^{(1)} \end{pmatrix}, \begin{pmatrix} a_{A,nm}^{(1)} + a_{C,nm}^{(1)} \\ b_{A,nm}^{(1)} + b_{C,nm}^{(1)} \end{pmatrix}, \begin{pmatrix} a_{A,nm}^{(1)} + a_{B,nm}^{(1)} + a_{C,nm}^{(1)} + a_{D,nm}^{(1)} \\ b_{A,nm}^{(1)} + b_{B,nm}^{(1)} + b_{C,nm}^{(1)} + b_{D,nm}^{(1)} \end{pmatrix}. \quad (3)$$

Case 1

Case 2

Case 3

Moreover, in the evaluation of the derivatives in the table, use is made of the general relation $d'_{r=r_k} \{r j_n(k_0 r)\} = j_n(k_0 r_k) + k_0 r_k j'_n(k_0 r_k)$, where $j'_n(x) = dj_n(x)/dx$.

The matrix \vec{M} is an 8-by-8 matrix which is obtained upon the application of the boundary conditions at the two CNP interfaces. Therefore, it depends on the values of the spherical waves (their radial dependencies) evaluated at the two interfaces. The explicit form of this matrix is found in [26, Equation

[†] The index $c = 3$ corresponds to the spherical Hankel functions of the first kind and order n ; it is not employed in the currently selected spherical vector wave expansion of the fields scattered from the CNP.

(9) and (10)]. The unknown expansion coefficients in (2) depend obviously on each EHD location and orientation. Once obtained, these coefficients yield a complete knowledge of the fields in all of the regions.

In our investigations of the properties of the active CNPs in the three excitation cases, the field solutions are used to examine the so-called normalized radiation resistance (NRR). The NRR represents the radiation resistance of the dipoles radiating in the presence of the CNP normalized by the radiation resistance of the dipoles radiating in free space, i.e., it is defined by

$$\text{NRR (dB)} = 10 \cdot \log_{10} \left(\frac{P_t}{P_{\text{EHD}}} \right), \quad (4)$$

where P_t is the total power radiated in the presence of the CNP for the Case 1, 2, and 3 excitations, and P_{EHD} is the power radiated by the EHDs in the corresponding excitation cases when they are situated in free space. The quantity P_t is given by the expression

$$P_t = \frac{\pi}{\omega k_0} \sum_{n=1}^{N_{\max}} \sum_{m=-n}^n 2 \frac{n(n+1)}{2n+1} \frac{(n+|m|)!}{(n-|m|)!} \left[\frac{|a_{nm}|^2}{\varepsilon_0} + \frac{|b_{nm}|^2}{\mu_0} \right], \quad (5a)$$

where the coefficients

$$a_{nm} = A_{4,nm} + \begin{cases} a_{A,nm}^{(4)} & \text{Case 1 ,} \\ a_{A,nm}^{(4)} + a_{C,nm}^{(4)} & \text{Case 2 ,} \\ a_{A,nm}^{(4)} + a_{B,nm}^{(4)} + a_{C,nm}^{(4)} + a_{D,nm}^{(4)} & \text{Case 3 ,} \end{cases} \quad (5b)$$

$$b_{nm} = B_{4,nm} + \begin{cases} b_{A,nm}^{(4)} & \text{Case 1 ,} \\ b_{A,nm}^{(4)} + b_{C,nm}^{(4)} & \text{Case 2 ,} \\ b_{A,nm}^{(4)} + b_{B,nm}^{(4)} + b_{C,nm}^{(4)} + b_{D,nm}^{(4)} & \text{Case 3 .} \end{cases}$$

The symbol N_{\max} in (5a) is the truncation limit in a numerical implementation of the infinite summation in the exact solution, and it is chosen such that the convergence in this expression is ensured. The quantity P_{EHD} , is given by (5) with $A_{4,nm} = B_{4,nm} = 0$. Because the EHDs are assumed to be excited as constant currents, the NRR is equal to the ratio of the total power radiated by the EHD in the presence of the CNP and in free space. Consequently, it is equivalent to the radiated power ratio introduced in the original metamaterial-based antenna studies [31–34] and the well-known Purcell factor [3, 35, 36] associated with spontaneous emission rates in a photonic environment.

In addition to the NRR values for various EHD-CNP configurations, the derived field solutions will also be used to study the power flow inside and outside of the CNP. This evaluation will be achieved in terms of the Poynting vector (both magnitude and direction)

$$\vec{S} = \frac{1}{2} \text{Re} \left\{ \vec{E} \times \vec{H}^* \right\} = \hat{a}_r S_r + \hat{a}_\theta S_\theta + \hat{a}_\phi S_\phi, \quad (6)$$

where S_r , S_θ , and S_ϕ are, respectively, its r -, θ -, and ϕ -components. These components of the Poynting vector are linked immediately to the different components of the total electric and magnetic fields [29].

3. BACKGROUND: CNP CASES

In several previous works [e.g., 6, 27] it has been shown that sub-wavelength optical CNPs can be designed with very large scattering cross-sections and total radiated power responses when gain is introduced into them. Moreover, these same active optical nano-particles have also been found to effectively reduce the total power radiated by the EHDs. The large responses obtained by these active CNPs are attributed to the excitation of a super-resonant state (resonant dipole mode), and the jamming capability is due to the excitation of the so-called non-radiating or jamming state of the entire system (these terms will be used interchangeably). To this end, the same CNP geometries studied in [4, Chap. 4, 27–29] are employed.

In all the cases presented below, the nano-core of the CNP consists of very low loss silica (treated here as lossless), and its nano-shell is a specific plasmonic material for which the size-dependency of its permittivity is taken into account [6]. The gain is introduced uniformly into the nano-core; it is modeled by a canonical, constant frequency, gain model. This means that the silica nano-core permittivity is represented as

$$\varepsilon_1 = (n^2 - \kappa^2 - 2jn\kappa) \varepsilon_0, \quad (7)$$

where $n = \sqrt{2.05}$ is the refractive index of the silica nano-core in the frequency region of interest, and the parameter κ determines the nature of the nano-core and thus of the CNP. Specifically, the nano-core is lossless and passive for $\kappa = 0$; it is lossy and passive for $\kappa > 0$; and it is active for $\kappa < 0$.

In the first set of investigation cases, the silica nano-core is covered with a silver (Ag) nano-shell. Three different CNP sizes were studied:

CNP A: $r_1 = 24$ nm, $r_2 = 30$ nm, $\kappa = -0.245$

CNP B: $r_1 = 16$ nm, $r_2 = 20$ nm, $\kappa = -0.274$

CNP C: $r_1 = 8$ nm, $r_2 = 10$ nm, $\kappa = -0.451$

cf., [4, Chap. 4], where the indicated values of the parameter κ were found to lead to the super-resonant states for these CNP configurations under a single EHD excitation. It is interesting to note that the amount of gain needed to overcome the absorption losses in the plasmonic material increases as the CNP size decreases. Thus, it can be inferred that the loss in the metal increases (i.e., the imaginary part of the permittivity is larger for smaller thicknesses). This behavior is important from a practical realization viewpoint, i.e., since the core size is also decreasing, it becomes more difficult to achieve higher κ values with a smaller amount of gain material.

In the second set of investigation cases, the silica nano-core radius is set to 24 nm, and the thickness of the plasmonic nano-shell is set to 6 nm. Three different plasmonic materials were examined: silver, gold (Au), and copper (Cu); the corresponding CNPs will be referred to as Ag-, Au-, and Cu-based CNPs. The gain constant for these cases were:

Ag-based CNP: $\kappa = -0.245$

Au-based CNP: $\kappa = -0.532$

Cu-based CNP: $\kappa = -0.741$

cf., [4, Chap. 4]. Again, the indicated values of the parameter κ lead to super-resonant states for these CNP configurations under a single EHD excitation. It is interesting to note that the largest (smallest) gain for overcoming the plasmonic absorption losses is needed in the Cu-based (Ag-based) CNP since copper (silver) is the most (least) lossy of the three plasmonic materials considered.

We note that while a dispersion-less refractive index is assumed for the gain region, the presented methodology enables a straightforward analysis of the maximum responses of the system. Moreover, if the entire dispersion engineering problem were considered, the goal would be to have both the resonances occur at the peak value of any dispersive gain model that is employed. As speculated and seen experimentally [8, 37–40] and as demonstrated theoretically [41, 42], the physical, bulk gain constants needed for the physical realization of gain-assisted nano-structures that exhibit extreme localization of the exciting fields in their gain regions and the corresponding resonance-enhanced scattering cross-sections are related to the effective values predicted directly from simulation, but are considerably less in reality because of those effects. The revised theoretical values, taking into account the impact of this resonant localization on the actual gain constants, are well within known values achieved by dyes [37], nanolasers [43] and quantum dots [44]. The corresponding κ values extracted from our analyses to achieve the super-resonant states can be realized from those systems.

4. RESULTS AND DISCUSSIONS

For both sets of cases, the NRR values were examined in detail. Those results were supplemented with intensity and near-field power flow distributions. The EHDs in all three excitation cases: Case 1, 2, or 3, were taken to be z -oriented, with the magnitudes of their individual dipole (current) moments set equal to 5 nA-m.

4.1. Influence of the Ag-based CNP Size: A , B, and C Super-resonant Designs

Figure 2 shows the NRR (dB) as a function of the excitation wavelength, λ , for the Case 1 (a), Case 2 (b) and Case 3 (c) excitations of all three super-resonant Ag-based CNP configurations, CNP A ($r_s = 40$ nm), CNP B ($r_s = 30$ nm), and CNP C ($r_s = 20$ nm). For all these excitation cases, rather profound maxima (peaks) of the NRRs are observed. These peaks are the signatures of the so-called super-resonances. Specifically, the NRR peak values are found to be around 63 dB (CNP A), 60 dB (CNP B), and 49 dB (CNP C). While the distance of the EHD from the outer surface of the CNP remains the same in all three cases, these peak values decrease as the total CNP size decreases because the smaller CNPs, despite being resonant, capture less of the EHD's incident power than the larger ones do. Moreover, as noted previously, the loss in a shell increases as it becomes thinner. Furthermore, one finds that as the size of the CNP decreases, the wavelength at which the super-resonance is achieved slightly detunes from 502.1 nm (CNP A) to 495.0 nm (CNP B) to 490.8 nm (CNP C).

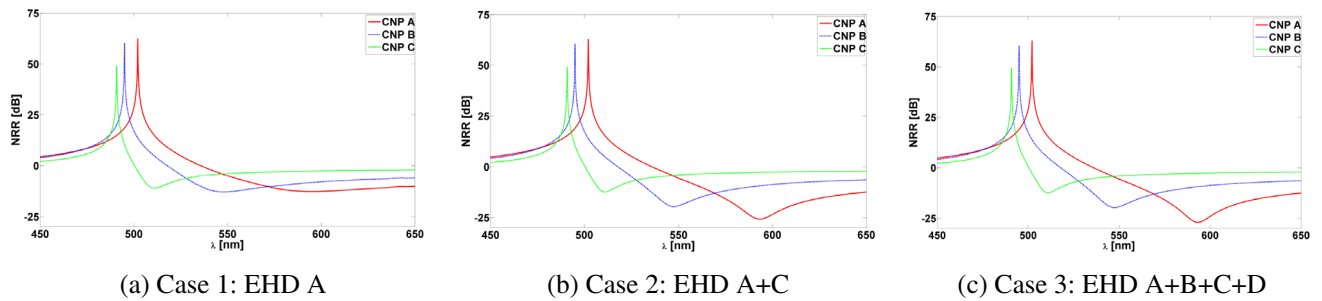


Figure 2. The NRR (dB) as a function of the excitation wavelength, λ , for the three CNP sizes for Case 1 (a), Case 2 (b), and Case 3 (c) excitations. The over-all radius (nano-shell thickness) is 30 nm (6 nm) for CNP A, 20 nm (4 nm) for CNP B, and 10 nm (2 nm) for CNP C. In all cases, the CNP's nano-cores are silica and the nano-shells are made of silver.

We also note that for a single EHD located *inside the core* of CNP A, B, and C, the corresponding magnitudes of the peak NRR value for all three CNP cases are comparable when their gain constants have been adjusted to achieve their maximum NRR values [27]. Even though the EHD field has complete access to all the gain material when it is located inside of a core, the cores of the smaller CNPs are volumetrically smaller. Again, their shells are thinner and, hence, they exhibit more loss. Consequently, there is the need for the larger gain constant as the CNP size becomes smaller. Since the ratio of the inner and outer radii is the same in all three cases, the net result is the comparable peak NRR values.

The super-resonant responses in the NRR curves reported in Figure 2 are physically due to the excitation of a strong resonant dipole mode inside the active CNPs. This enhanced response results from a pole in the expansion coefficients (2) of the scattered field outside the CNP. More specifically, it corresponds to a pole of the TM expansion coefficient $A_{4, nm}$. With reference to [26, Equation (15a)], we recall that the juxtaposition of materials with oppositely signed permittivities is required to “establish” a pole of the said expansion coefficients for electrically small structures and, thus, to attain the super-resonant behavior. This necessary ingredient is present in all of the configurations considered in virtue of the silica nano-core, which has positive permittivity, and the silver nano-shell, which has a negative real part of its permittivity in the investigated wavelength regime [6, 27].

The near-field behavior of the single EHD case excitation was illustrated elsewhere [27]. In a similar manner, we illustrate the super-resonance behaviors in the Case 3 excitation (EHD A+B+C+D) of the Ag-based CNP A, B, and C cases in Figure 3. The magnitude and direction of the Poynting vector (6) in both the E (xz) and H (xy) planes corresponding to the peaks in Figure 2(c) are presented. The color shows the magnitude of the Poynting vector defined as $10 \log_{10} |\vec{S}/1(\text{W/m}^2)|$ and the arrows depict the direction of the Poynting vector.

These results are rather illustrative as they demonstrate, for instance, whether the power is incoming or outgoing relative to the CNP and the surrounding emitters. Note that the four EHDs are located 10 nm away from the CNP at their respective positions for all three cases. In all three cases, it is

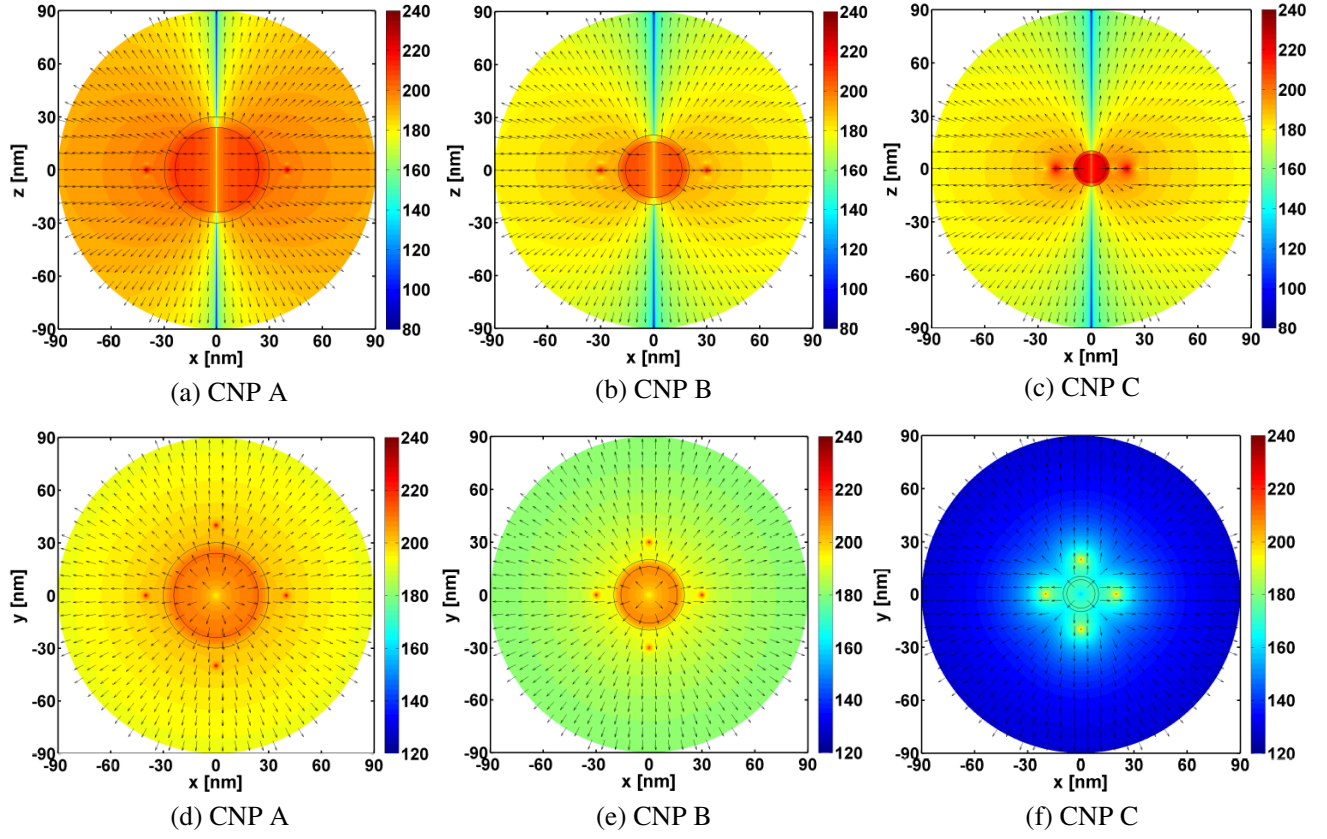


Figure 3. Magnitude (color) and direction (arrows) of the power flow for the Case 3 (EHD A+B+C+D) excitations of the super-resonant Ag-based CNP A case ((a), (d)), CNP B case ((b), (e)), and CNP C case ((c), (f)). These results correspond to the NRR *peaks* in Figure 2(c). The power flow is shown in the xz -plane (E -plane) in the upper-row Figures (a)–(c), and in the xy -plane (H -plane) in the lower-row figures (d)–(f). In both planes the results are shown in a circular region of radius equal to 90 nm. In all cases the EHDs are located in the exterior of the CNP in the xy -plane at $r_s = 40$ nm (CNP A), $r_s = 30$ nm (CNP B), and $r_s = 20$ nm (CNP C). The curves representing the spherical surfaces of the CNP are also shown. Note that results identical to those in the xz -plane are also obtained in the yz -plane where the two other EHDs, EHD B and D, are located. Only the EHDs A and C are visible in (a)–(c), whereas all four EHDs are visible in (d)–(f).

clear that the large NRR values correspond to the excitation of a strong resonant dipole mode. While the direction of the Poynting vector in all cases indicates a similar dipolar outward power flow, its magnitude reveals that the dipole mode is most strongly excited in the largest CNP, CNP A, as seen in Figures 3(a) and (d). On the other hand, this response diminishes as the particle size decreases. This behavior is clearly seen for the CNP C case in Figures 3(c) and (f).

Apart from the profound peaks, the NRR values are also found in Figure 2 to exhibit minima (dips) in their behavior at specific wavelengths. Whereas the super-resonance wavelengths detune only slightly towards lower values as the CNP size decreases, the minimum values (dips) of the NRR, which correspond to the jamming state [4 Chap. 4, 27, 29], are found to shift significantly to lower wavelengths. The dips are substantially deeper as the number of emitters increases from one to more, except for CNP C. Moreover, the magnitudes of the dips are approximately the same for the Case 1 excitation for the three CNP sizes. On the other hand, they significantly decrease as the size of the CNP decreases for the Case 2 and 3 excitations. Thus, while the jamming levels of a single quantum emitter are comparable for all three CNP sizes, efficient jamming of multiple emitters is found to require the larger particle sizes for the emitter locations presently investigated. This behavior reflects the decrease in the overall resonant response noted in Figure 2 as the CNP size decreases. The minima of the NRR

Table 2. Minimum NRR values (dB) and the corresponding wavelengths (nm) for the Cases 1, 2, and 3 EHD excitations for different sizes of the Ag-based CNP. The EHDs are outside the CNP at $r_s = 40$ nm (CNP A), 30 nm (CNP B), and 20 nm (CNP C).

CNP	Excitation case		
	1	2	3
A	-12.7 dB	-25.8 dB	-27.1 dB
	594.9 nm	593.2 nm	593.2 nm
B	-13.0 dB	-19.6 dB	-19.8 dB
	547.7 nm	547.4 nm	547.4 nm
C	-11.0 dB	-12.5 dB	12.5 dB
	510.9 nm	510.9 nm	510.9 nm

(dB) and the wavelengths at which they are attained are summarized in Table 2 for the three particle sizes and the different excitation cases.

The dips in the NRR values reported in Figure 2 correspond to the excitation of non-resonant, non-radiating (dark) states. These states are analogous to the transparency/cloaking effects introduced in, e.g., [15, 20]. However, whereas in the cloaking case where the scattering coefficients go to zero to preserve the incident field, the non-radiating state occurs here because the resonant CNP cancels out the EHD fields yielding total field coefficients near zero (alternatively, as a total system, the active CNP effectively cloaks the presences of the EHDs). Consequently, these dips are a non-resonant effect and, hence, are broader in wavelength than the super-resonances are.

To connect the multiple source behavior of these dips with the Ag-based CNP A case results reported in [29], Figure 4 shows the magnitude and direction of the Poynting vector (6) in the $H(xy)$ plane corresponding to the dips in Figure 2(c). In all cases, the four EHDs are located 10 nm away from the CNP at their respective positions, and the power flow is shown in an enlarged circular region of 180 nm radius which completely encloses the emitters and the CNP. These results clearly show that the power flow throughout most of this region around the CNP is inwards, towards the CNP. Even though it is hard to notice from Figure 4, it was verified that the active CNP nano-core itself acts, however, like an effective dipole source with an outward power flow. The overall inward power flow behavior observed in Figure 4 indicates that the active CNP, when excited by the emitters, has actually created field values for $r > r_s$ that are in opposition to and exceed those of the EHDs. A sink-like behavior of the overall power flow is thus created which decreases the net outward power flow. Consequently, a large portion of the radiated power is confined in this region, preventing it from ever reaching the far-field. This explains the reduced NRR values reported in Figure 2. The spherical region in which this sink-like behavior is found, is largest for the largest CNP case. It gets progressively smaller as the CNP size decreases. In particular; its thickness is around 145 nm, 105 nm, and 75 nm, respectively, for the CNP A, CNP B, and CNP C cases. This effect is analogous to the impact that the CNP size has on the super-resonance behavior of the NRR peak values. The larger CNP simply captures more of the power emitted by the EHDs, thus producing larger field values that result in the net inward power flow. Note that while there is an outward power flow in all of the figures in the region outside of the sink-like region, it is significantly smaller than the values would be if only the four emitters were present. Also note that if one were to take a spherical shell that is symmetrical in thickness about the region which defines the boundary between the sink- and source-like regions outside of the locations of the CNPs and the emitters in Figure 4, the inward power flow through its inner surface and outward power flow through its outer surface would yield a very small outward net total power value. Again, this value is much smaller than would be obtained if only the emitters were present. This result is yet another clarification of the nulls shown in Figure 2.

It is also important to emphasize that the jamming phenomena reported here is not due to losses inside the CNP. On the contrary, the presence of the gain helps provide the appropriate field distribution scattered by the CNP that decreases the net outward flow of power, thus leading to the observed dips in the NRR values. We have confirmed these explanations in [29] by contrasting the responses for single

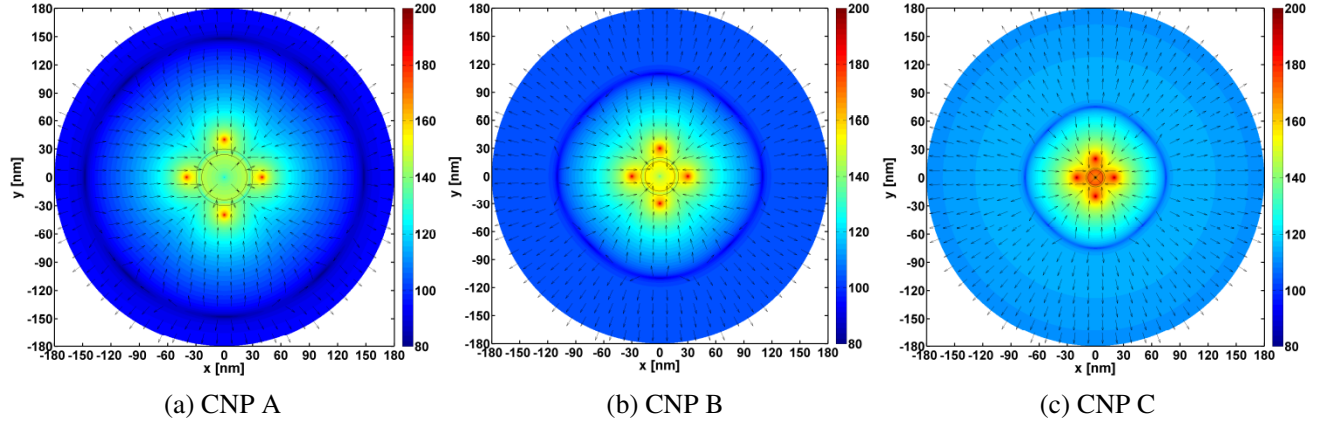


Figure 4. Magnitude (color) and direction (arrows) of the power flow for Case 3 (EHD A+B+C+D) excitations of the jamming case of the Ag-based CNP A (a), CNP B (b), and CNP C (c). These results correspond to the NRR *dips* in Figure 2(c). The power flow is shown in the xy -plane (H -plane) in a circular region of radius equal to 180 nm. In all cases the EHDs are located in the exterior of the CNP in the xy -plane at $r_s = 40$ nm (CNP A), $r_s = 30$ nm (CNP B), and $r_s = 20$ nm (CNP C), thus maintaining the relative distance between the EHDs and the CNPs at 10 nm in all cases. Curves representing the spherical surfaces of the CNP are also shown.

emitter excited, passive and active Ag-based CNPs.

Extensive studies were performed on the influence of the emitter locations on the NRR peaks and dips. The NRR peaks were gradually reduced as the distance between the CNP and the emitters was increased due to the decreased coupling between the emitters and the CNP. In all cases, the most extreme variation of the depth of the dips occurred in the transition between the one and two emitter cases. The dips were found to be generally deeper as the distance between the emitters and the CNP decreased, and they occurred at larger wavelengths. In all cases the absolute value of the NRR dips for the same relative CNP-emitter distances was largest for the largest CNP sizes, in line with the above observations. Moreover, the largest CNP, CNP A, provided the largest dynamic range of operation, i.e., the difference between the peak and the dip NRR values, for all investigated emitter locations.

We note that these results were obtained for the values of κ which yielded the super-resonant behaviors, i.e., the peak NRR values. We have also investigated the effect of this parameter on the enhancement and jamming levels for all three particles sizes. In general, the super-resonant NRR peaks are extremely sensitive to even slight variations of this parameter, and they drop by several orders of magnitude for even small deviations from when κ is varied away from its super-resonance value. The NRR dips are also affected in a similar manner by this parameter, but not nearly as much as the peaks since they are non-resonant behaviors. The super-resonant designs were found to lead to the largest dynamic range in the NRR values in all cases.

4.2. Influence of the Material Choice: Ag-, Au- and Cu-based CNP A Super-resonant Designs

We also investigated the influence of the plasmonic-material choice on the enhancement and jamming levels for the three excitation cases in the CNP A configuration (i.e., 24 nm radius core and 6 nm thick shell). The EHDs are located at $r_s = 40$ nm. Figure 5 shows the NRR values (dB) as a function of the excitation wavelength, λ , for the Case 1 (a), Case 2 (b) and Case 3 (c) excitations of the Ag-, Au-, and Cu-based CNP configurations.

Regardless of the excitation case, the peak value of the NRR is around 63 dB (Ag-based CNP), 64 dB (Au-based CNP), and 59 dB (Cu-based CNP). The wavelengths at which the peaks occur increase significantly when silver is replaced with gold, and only slightly with the replacement of gold with copper. All of these observations are in line with our previous analyses performed for the special case of a single EHD [4 Chap. 4, 28]. We reiterate that these super-resonant behaviors are associated with

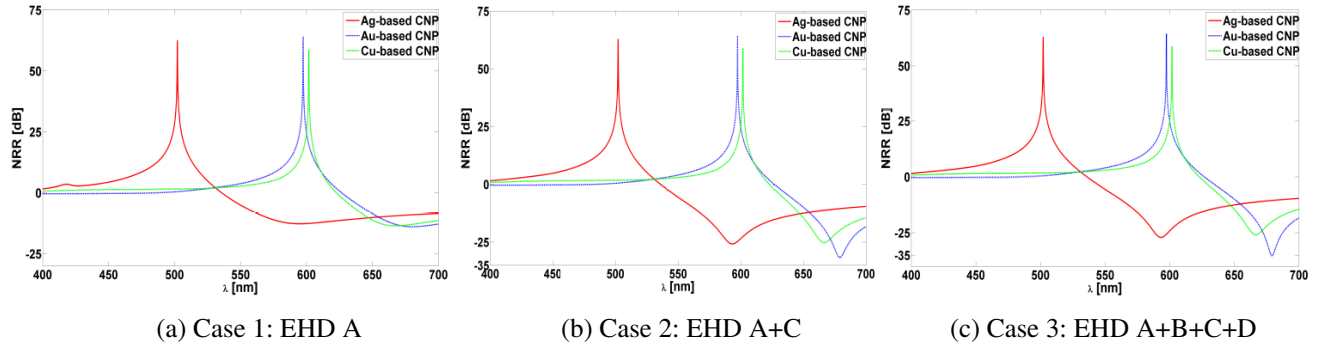


Figure 5. The NRR values (dB) as a function of the free-space wavelength, λ , for the Ag-, Au-, and Cu-based CNPs for Case 1 (a), Case 2 (b), and Case 3 (c) excitations. The over-all radius (nano-shell thickness) for all CNPs is 30 nm (6 nm). Their 24 nm radius silica nano-core is impregnated uniformly with the gain material.

the fundamental dipole resonances of the active CNPs. Although not included in here, similar results were obtained for the other two plasmonic material choices. While silver has a lower loss than gold at optical wavelengths, it was found that the resonant dipole mode of the Au-based CNPs produced the largest response. This behavior occurred because of the significantly larger gain constant used to obtain the Au-based super-resonance states.

The minimum values of the NRR are also found to shift to much larger wavelengths when the silver nano-shell is replaced with one that is either gold or copper. Moreover, for all material choices, the NRR dips are found to be deeper as the number of EHDs increases. This behavior is most apparent when going from 1 to 2 EHDs, whereas the increase is less notable when going from 2 to 4 EHDs. The magnitudes of the NRR dips are, for all excitation cases, comparable for the Ag- and Cu-based CNPs. Moreover, for the Case 1 excitation, these magnitudes are also of the same order for all three plasmonic material choices. However, as the number of quantum emitters increases, the Au-based CNPs are found to offer dip values that clearly surpass those of the Ag- and Cu-based CNPs. The minima for the Au-based CNPs are found to be around -32 dB for the Case 2 excitation (Figure 5(b)), and around -35 dB for the Case 3 excitation (Figure 5(c)). Thus, when compared with the Ag- and Cu-based CNP designs, the Au-based CNP provides the strongest super-resonance states (manifested in the largest NRR levels) and the strongest jamming levels (manifested in the smallest NRR levels). Combining these conclusions with those from Section 4.1, it follows that efficient enhancement, as well as jamming of the quantum emitter radiation, requires Au-based CNPs of larger sizes. These findings are particularly notable when multiple quantum emitters (EHDs) are located in the proximity of the active CNP. The minima of the NRR (dB) and the wavelengths at which they are attained are summarized in Table 3 for the Ag-, Au-, and Cu-based CNPs.

Table 3. Minimum NRR values (dB) and the corresponding wavelengths (nm) for the Case 1, 2, and 3 EHD excitations for different sizes of the Ag-, Au-, and Cu-based CNPs whose size is that of the CNP A configuration ($r_1 = 24$ nm, $r_2 = 30$ nm). The EHDs are located exterior to the CNPs at 40 nm.

CNP	Excitation case		
	1	2	3
Ag	-12.7 dB	-25.8 dB	-27.1 dB
	594.9 nm	593.2 nm	593.2 nm
Au	-13.9 dB	-31.7 dB	-35.2 dB
	680.7 nm	679.1 nm	679.1 nm
Cu	-13.5 dB	-25.4 dB	-25.9 dB
	667.3 nm	666.5 nm	666.5 nm

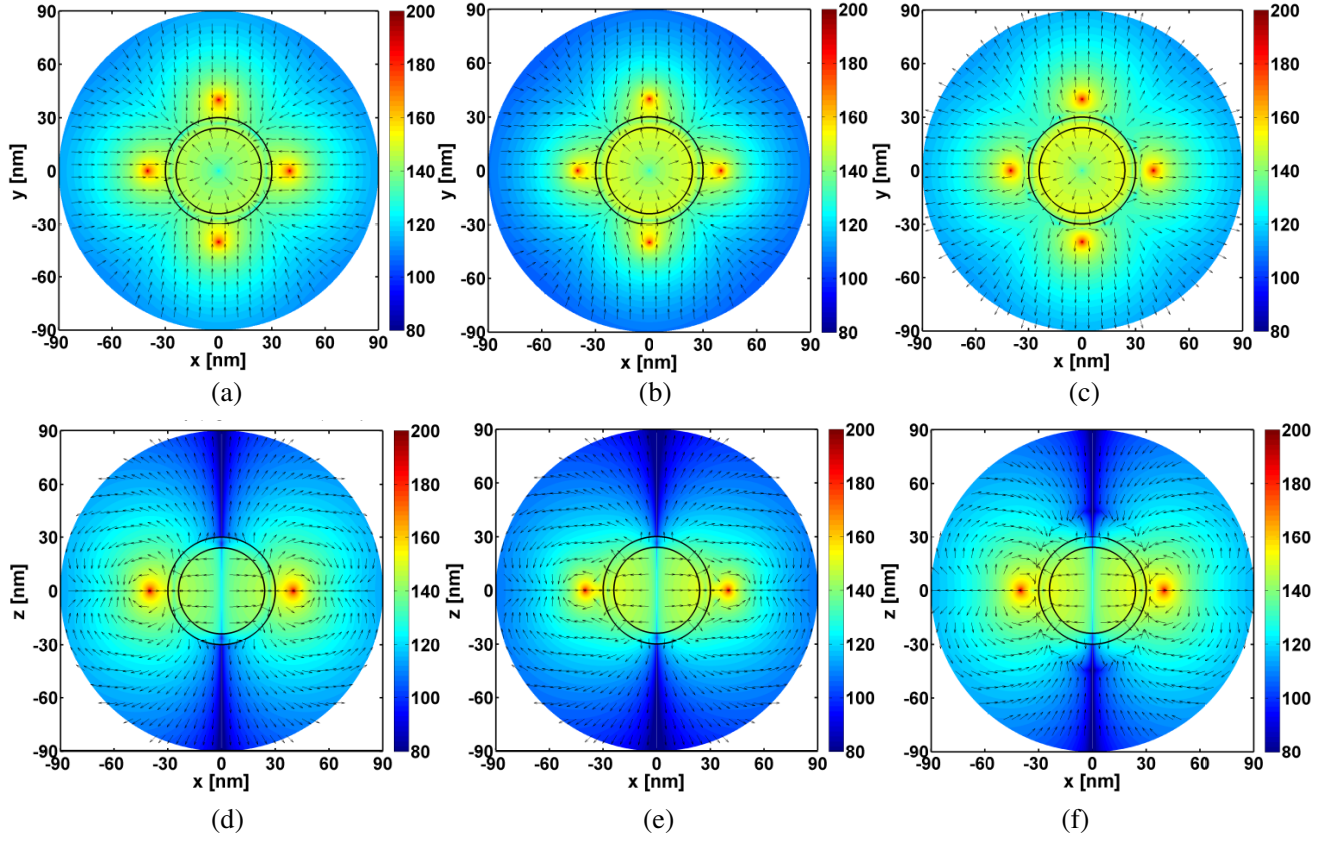


Figure 6. Magnitude (color) and direction (arrows) of the power flow for Case 3 excitations of the Ag-based CNP, (a) and (d); Au-based CNP, (b) and (e); and Cu-based CNP, (c) and (f). The upper-row of the figure shows the power flow in the xy -plane (H -plane), and the lower-row shows it in the xz -plane (E -plane). In both planes the results are shown in a circular region of radius equal to 90 nm. In all cases the EHDs are located in the exterior of the CNP in the xy -plane at $r_s = 40$ nm. The curves representing the spherical surfaces of the CNP are shown in each subplot. Note that results identical to those in the xz -plane are also obtained in the yz -plane where the two other EHDs, EHD B and D, are located.

The field behaviors at the NRR dips reported in Figure 5 are briefly illustrated via their power flows for the Case 3 excitation, which are shown in Figure 6 for the super-resonant Ag-based CNP, (a) and (d); Au-based CNP, (b) and (e); and Cu-based CNP, (c) and (f). Again, the color depicts the power flow magnitude while the arrow shows its direction. The figures in the upper-row depict the results in the xy -plane (H -plane), and the figures in the lower-row depict the results in the xz -plane (E -plane). The E -plane shown here includes the EHDs A and C. The same results are obtained in the other E -plane, yz -plane, for the EHDs B and D; and they are, therefore, not included here. Both the H - and E -plane results in all cases show that the active CNP nano-core acts like an effective dipole source with a power flow that is directed away from the CNP centers. In the exterior of the CNPs, the directions of the power flow are similar for the Ag- and Au-based CNPs in both the H - and E -planes, while it is different for the Cu-based CNP. These H -plane results clearly show that the power flow is inwardly directed for the Ag- and Au-based CNPs, i.e., the entire four-EHD/CNP system acts like an effective sink. The corresponding E -plane results in Figures (d) and (e) show a power flow which is mostly outward, away from the CNP, but becomes inward towards it along the positive and negative x -axis. In contrast, the H -plane results for the Cu-based CNP show an outwardly directed power flow, while the associated E -plane results present a stronger inward power flow. This suggests that the Cu-based CNP also acts as an effective sink for any external power flow. These behaviors, and thus the fundamental physics behind the jamming state, conform to the analysis presented above in Section 4.1. Even though not shown here, the magnitudes of the power flow reported in Figure 6 are significantly

below the corresponding ones of the EHDs situated alone in free space. This fact further confirms the jamming capabilities of these active CNPs, where appropriate field distributions are created to prevent an outward power flow from the EHDs.

5. SUMMARY AND CONCLUSIONS

The ability of several different classes of active CNPs to enhance or jam the total power radiated from multiple quantum emitters was demonstrated. Various sizes and plasmonic coatings of the CNPs provided insights into their response levels and the capabilities to tune both their enhanced and jamming states. Increasing the number of quantum emitters in the vicinity of the properly designed, resonant, active CNPs led to unexpected larger decreases in the minimum NRR values. This was most emphasized for the Au-based CNPs. Moreover, it was found that for multiple EHD excitations, the most efficient jamming requires larger particle sizes. The Au-based CNP also provided the strongest enhancements of the NRR. The super-resonance states, which result from the highly tuned geometries and the singular-like (pole) behaviors of the scattering coefficients, were found to have narrower bandwidths than their jamming states for which the active CNP cancels out the EHDs fields yielding total field coefficients near zero. It also was demonstrated that the active CNP jammers acts as strong sinks to any exterior power flow. These enhancement and jamming characteristics can be exploited to facilitate high resolution chemical and molecular fluorescent essays. We note that these conclusions were obtained when the gain constants were adjusted to achieve the largest NRR values. The gain constant was the smallest (largest) for the Ag-based (Cu-based) cases. If the gain constant was restricted to the Ag-case value, the lower loss Ag-based CNPs would be the best choices to observe the resonant enhancement and jamming effects for the configurations considered in this work.

While we reported results for the phase coherent and like polarization responses of all of the emitters to illustrate the maximum response behaviors, we have studied the effects of partial and incoherent multiple emitters, as well as the effects of the orientations of those emitters. These results have been reported elsewhere [45]. While the coherence of the phases and orientations of the emitters does impact the levels of enhancement and jamming, those effects remain and can be exploited even in such practical environments.

As noted at the start, canonical problems described by Maxwell's equations have provided insights into the physics underlying a variety of electromagnetic phenomena over the last 150 years. In future works we will examine the enhancement and jamming levels for quantum emitters when they are coupled to eccentrically-layered and multi-layered concentric, active CNPs, as well as to appropriately arranged clusters of the CNPs investigated in the present work. These more complex canonical problems will continue to elucidate the underlying physic and potential benefits of active core-shell configurations in fluorescence, nano-antennas and other optical and photonics applications.

ACKNOWLEDGMENT

This work was supported in part by NSF contract number ECCS-1126572.

REFERENCES

1. Cai, W. and V. Shalaev, *Optical Metamaterials*, Springer, Berlin, Germany, 2010.
2. Gordon, J. A. and R. W. Ziolkowski, "CNP optical metamaterials," *Opt. Express*, Vol. 16, 6692–6716, Apr. 2008.
3. Bharadwaj, P., B. Deutsch, and L. Novotny, "Optical antennas," *Adv. Opt. Photon.*, Vol. 1, No. 3, 438–483, 2009.
4. Agio, M. and A. Alù, *Optical Antennas*, Cambridge University Press, New York, 2013.
5. Klar, T. A., A. V. Kildishev, V. P. Drachev, and V. M. Shalaev, "Negative-index metamaterials: Going optical," *IEEE J. Sel. Topics Quantum Electron.*, Vol. 12, No. 6, 1106–1115, Nov./Dec. 2006.
6. Gordon, J. A. and R. W. Ziolkowski, "The design and simulated performance of a coated nanoparticle laser," *Opt. Express*, Vol. 15, No. 5, 2622–2653, Mar. 2007.

7. Gordon, J. A. and R. W. Ziolkowski, "Investigating functionalized active coated nano-particles for use in nano-sensing applications," *Opt. Express*, Vol. 15, No. 20, 12562–12582, Oct. 2007.
8. Xiao, S., V. P. Drachev, A. V. Kildishev, X. Ni, U. K. Chettiar, H.-K. Yuan, and V. M. Shalaev, "Loss-free and active optical negative-index metamaterials," *Nature*, Vol. 466, No. 7307, 735–738, Aug. 2010.
9. De Luca, A., M. P. Grzelczak, I. Pastoriza-Santos, L. M. Liz-Marzán, M. La Deda, M. Striccoli, and G. Strangi, "Dispersed and encapsulated gain medium in plasmonic nanoparticles: A multipronged approach to mitigate optical losses," *ACS Nano*, Vol. 5, No. 7, 5823–5829, 2011.
10. Klopfer, M. and R. K. Jain, "Plasmonic quantum dots for nonlinear optical applications," *Opt. Mat. Express*, Vol. 1, No. 7, 1353–1366, Oct. 2011.
11. Campione, S., M. Albani, and F. Capolino, "Complex modes and near-zero permittivity in 3D arrays of plasmonic nanoshells: Loss compensation using gain," *Opt. Mat. Express*, Vol. 1, No. 6, 1077–1089, Oct. 2011.
12. Pan, J., Z. Chen, J. Chen, P. Zhan, C. J. Tang, and Z. L. Wang, "Low-threshold plasmonic lasing based on high- Q dipole void mode in a metallic nanoshell," *Opt. Lett.*, Vol. 37, No. 7, 1181–1183, Apr. 2012.
13. Li, Z.-Y., "Metal nanoparticles with gain toward single-molecule detection by surface-enhanced raman scattering," *Nano Lett.*, Vol. 10, 243–249, 2010, doi: 10.1021/nl903409x.
14. Liu, S.-Y., J. Li, F. Zhou, L. Gan, and Z.-Y. Li, "Efficient surface plasmon amplification from gain-assisted gold nanorods," *Opt. Lett.*, Vol. 36, No. 7, 10146–9592, Apr. 2011.
15. Alù, A. and N. Engheta, "Achieving transparency with plasmonic and metamaterial coatings," *Phys. Rev. E*, Vol. 72, 017723, Jul. 2005.
16. Strangi, G., A. De Luca, S. Ravaine, M. Ferrie, and R. Bartolino, "Gain induced optical transparency in metamaterials," *Appl. Phys. Lett.*, Vol. 98, No. 25, 251912, Jun. 2011.
17. Chew, H. W., P. J. McNulty, and M. Kerker, "Model for a Raman and fluorescent scattering by molecules embedded in small particles," *Phys. Rev. A*, Vol. 13, 396–404, 1976.
18. Gordon, J. A. and R. W. Ziolkowski, "Investigating functionalized active coated nano-particles for use in nano-sensing applications," *Opt. Express*, Vol. 15, 12562–12582, Oct. 2007.
19. Alexopoulos, N. G. and N. K. Uzungolu, "Electromagnetic scattering from active objects: Invisible scatterers," *Appl. Opt.*, Vol. 17, 235–232, 1978.
20. Alù, A. and N. Engheta, "Plasmonic and metamaterial cloaking: Physical mechanisms and potentials," *J. Opt. A: Pure Appl. Opt.*, Vol. 10, 2008, doi: 10.1088/1464-4258/10/9/093002.
21. Xu, Q., F. Liu, W. Meng, and Y. Huang, "Plasmonic core-shell metal-organic nanoparticles enhanced dye-sensitized solar cells," *Opt. Express*, Vol. 20, No. 106, A898–A907, Nov. 2012.
22. Alù, A. and N. Engheta, "Enhanced directivity from subwavelength infrared/optical nano-antennas loaded with plasmonic materials or metamaterials," *IEEE Trans. Antennas Propagat.*, Vol. 55, 3027–3039, Nov. 2007.
23. Hirsch, L. R., A. M. Gobin, A. R. Lowery, F. Tam, R. A. Drezek, N. J. Halas, and J. L. West, "Metal nanoshells," *Ann. Biomed. Eng.*, Vol. 34, No. 1, 15–22, Jan. 2006.
24. Halas, N. J., "Plasmonics: An emerging field fostered by nano letters," *Nano. Lett.*, Vol. 10, 3816–3822, Sep. 2010.
25. Choi, I. and Y. Choi, "Plasmonic nanosensors: Review and prospect," *IEEE J. Selected Top. Quantum Electron.*, Vol. 18, No. 3, 1110–1121, May/June. 2012.
26. Arslanagić, S., R. W. Ziolkowski, and O. Breinbjerg, "Radiation properties of an electric Hertzian dipole located near-by concentric metamaterial spheres," *Radio Sci.*, Vol. 42, RS6S16, Nov. 2007, doi:10.1029/2007RS003663.
27. Arslanagić, S. and R. W. Ziolkowski, "Active coated nano-particle excited by an arbitrarily located electric Hertzian dipole — Resonance and transparency effects," *J. Opt. A*, Vol. 12, 024014, Feb. 2010.
28. Arslanagić, S. and R. W. Ziolkowski, "Active coated nano-particles: Impact of plasmonic material choice," *Appl. Phys. A*, Vol. 103, 795–798, Jun. 2011.

29. Arslanagić, S. and R. W. Ziolkowski, "Jamming of quantum emitters by active coated nanoparticles," *IEEE J. Selected Top. Quantum Electron.*, Vol. 19, No. 3, 4800506, May/June 2013.
30. Chance, R. R., A. Prock, and R. Silbey, "Molecular fluorescence and energy transfer near interfaces," *Adv. Chem. Phys.*, Vol. 37, 1–65, 1978.
31. Ziolkowski, R. W. and A. D. Kipple, "Reciprocity between the effects of resonant scattering and enhanced radiated power by electrically small antennas in the presence of nested metamaterial shells," *Phys. Rev. E*, Vol. 72, 036602, Sep. 2005.
32. Ziolkowski, R. W. and A. Erentok, "Metamaterial-based efficient electrically small antennas," *IEEE Trans. Antennas Propagat.*, Vol. 54, 2113–2130, Jul. 2006.
33. Erentok, A. and R. W. Ziolkowski, "A hybrid optimization method to analyze metamaterial-based electrically small antennas," *IEEE Trans. Antennas Propagat.*, Vol. 55, No. 3, 731–741, Mar. 2007.
34. Ziolkowski, R. W. and A. Erentok, "At and beyond the Chu limit: Passive and active broad bandwidth metamaterial-based efficient electrically small antennas," *IET Microwaves, Antennas & Propagation*, Vol. 1, No. 1, 116–128, Feb. 2007.
35. Purcell, E. M., "Spontaneous emission probabilities at radio frequencies," *Phys. Rev.*, Vol. 69, 681, Jun. 1946.
36. Novotny, L. and B. Hecht, *Principles of Nano-optics*, Cambridge University Press, New York, 2012.
37. Noginov, M. A., G. Zhu, A. M. Belgrave, R. Bakker, V. M. Shalaev, E. E. Narimanov, S. Stout, E. Herz, T. Suteewong, and U. Wiesner, "Demonstration of a spaser-based nanolaser," *Nature Photon.*, Vol. 460, 1110–1112, Aug. 2009.
38. Noginov, M. A., G. Zhu, V. P. Drachev, and V. M. Shalaev, "Surface plasmons and gain media," *Nanophotonics with Surface Plasmons*, Chap. 5, 141–169, Elsevier, 2007.
39. Sivan, Y., S. Xiao, U. K. Chettiar, A. V. Kildishev, and V. M. Shalaev, "Frequency-domain simulations of a negative-index material with embedded gain," *Opt. Express.*, Vol. 17, 24060–24074, Dec. 2009.
40. Fang, A., T. Koschny, and C. M. Soukoulis, "Lasing in metamaterial nanostructures," *J. Opt.*, Vol. 12, 024013, Jan. 2010.
41. Campbell, S. D. and R. W. Ziolkowski, "Impact of strong localization of the incident power density on the nano-amplifier characteristics of active coated nano-particles," *Opt. Commun.*, Vol. 285, No. 16, 3341–3352, 2012.
42. Li, D. B. and C. Z. Ning, "Giant modal gain, amplified surface plasmon-polariton propagation, and slowing down of energy velocity in a metal-semiconductor-metal structure," *Phys. Rev. B*, Vol. 80, 153304, Oct. 2009.
43. Hill, M. T., "Status and prospects for metallic and plasmonic nano-lasers [invited]," *J. Opt. Soc. Am. B*, Vol. 27, B36–B44, Nov. 2010.
44. Campbell, S. D. and R. W. Ziolkowski, "The performance of active coated nanoparticles based on quantum dot gain media," *Adv. Optoelectron.*, Vol. 2012, Article ID 368786, 2012.
45. Arslanagić, S. and R. W. Ziolkowski, "Nano-sensing of the orientation of fluorescing molecules with active coated nano-particles," *Photonics and Nanostructures — Fundamentals and Applications*, Feb. 2014.